In vivo Hyperspectral Imaging of Microvessel Response to Trastuzumab Treatment in Breast Cancer Xenografts

By

Devin Rei McCormack

Thesis

Submitted to the Faculty of the

Graduate School of Vanderbilt University

In partial fulfillment of the requirements

For the degree of

MASTER OF SCIENCE

in

Biomedical Engineering

August, 2014

Nashville, Tennessee

Approved:

Melissa C. Skala, Ph.D.

Craig L. Duvall, Ph.D.

ACKNOWLEDGEMENTS

Funding sources that supported this work include NIH R00-CA142888, VICC Young Ambassadors Discovery Grant, NCI Breast Cancer SPORE P50-CA098131, and AHA Greater Southeast Affiliate Pre-doctoral Fellowship. Histological experiments were performed with assistance from the Vanderbilt Translational Pathology Shared Resource (supported by Cancer Center Support Grant 5P30 CA068485). Many thanks to Alex Walsh for help with cell work and treatments, Wesley Sit for assisting with animals, Kristin Poole for help with hyperspectral system design, Dr. Rebecca Cook and Dr. Jin Chen for lending their expertise on tumor biology, Dr. Carlos Arteaga for allowing usage of his cell lines, and Andrew Fontanella for assistance with vascular image processing. I would like to additionally thank other members of the Optical Imaging Laboratory; including Dr. Chetan Patil, Jason Tucker-Schwartz, and Amy Shah for their support and knowledge they shared during this project. Finally, I would like to thank my parents, Dr. Guy and Norma McCormack as well as my brother Guyon for continuing support in my academic endeavors.

TABLE OF CONTENTS

Page

LIST OF TABLES

Table Page

LIST OF FIGURES

Figure Page

CHAPTER 1

INTRODUCTION

Angiogenesis and the Vascular Network

Vascular Growth and Function

Blood vessels exist as an extensive network of supply conduits, and have the crucial role of nurturing all the tissues of the body. Initiation of the blood vessel network begins in the embryo, with an assembly of endothelial precursors that differentiate into a primitive vascular network through a process called vasculogenesis (Figure 1)[1]. Further maturation and infiltration of the vascular network is accomplished through angiogenesis, or vascular sprouting and remodeling, and finally expansion and stabilization through arteriogenesis[2]. Once fully grown, these processes are in a quiescent state in most organisms and tissues.

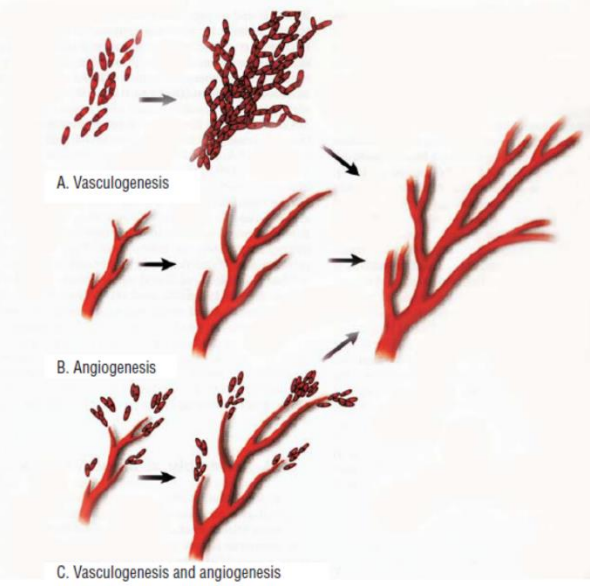

Figure 1: Schematic representation of angiogenesis and vasculogenesis. Angiogenesis is the formation of blood vessels from pre-existing vessels by proliferation of differentiated cells[3].

In healthy adults, vascular morphology and density are relatively static with minimal remodeling and generation. The vasculature is also remarkably adaptable, allowing for adequate blood flow to meet the dynamic metabolic demands of the body. However, regulation of vascularization is still crucial in cases of extreme disruption, and vascular damage is quickly met with a cascade of physiological processes resulting in angiogenesis to compensate for local hypoxia. Due to vascular stability in adulthood under normal conditions, angiogenesis is almost exclusively associated with injury and pathology[4], and an understanding of the events that lead to vascular growth and remodeling can provide insight into a wide range of diseases. Increased angiogenesis is involved in the pathological processes of cancer, thrombosis, and inflammatory disorders. Although the consequences of pathological vasculature are well known, the process of vascularization itself a complex orchestration of signaling and events that is not fully understood.

Abnormal Vasculature in the Tumor Microenvironment

In solid tumors, angiogenesis is required for continued growth and metastasis[5]. However, angiogenesis in tumors results in structurally and functionally abnormal vasculature due to an imbalance of pro- and anti-angiogenic factors (Figure 2)[6]. Poorly formed vasculature does little to alleviate hypoxic stress in the tumor mass, resulting in a continuous effort by the tumor mass to stimulate angiogenesis. Vascular normalization has become a guiding concept in tumor microenvironment therapy[7]. Gold standard immunohistochemical methods to determine vascularization suffer from single time-point measurement of a highly dynamic process[8], [9]. Longitudinal methods such as PET[10], CT[11], and MRI[12], [13] do not have sufficient resolution to detect microvascular structures. Development of methods to longitudinally describe the extent of abnormal microvascular structure and function within the tumor is valuable to study of vascular normalization.

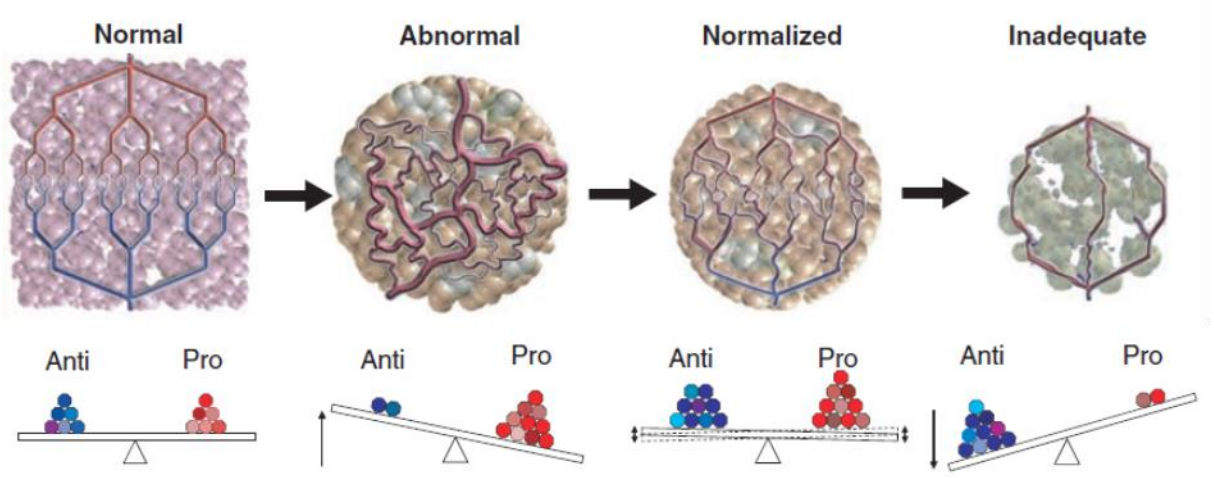

Figure 2: Vascular normalization with anti-angiogenic therapy. Anti-angiogenic therapy seeks to balance the angiogenic processes without over treating[14].

Breast Tumor Treatment with Trastuzumab

HER2 Overexpression in Breast Tumors

HER2 encodes a transmembrane *erb*B growth factor receptor high homologous to EGFR[15]. HER2 has no known ligand, but heterodymerizes with HER3 and HER4, which bind to heregulin. Heregulin is active in the PI3K-AKT pathway, related to proliferation and cell survival[16]. Through this pathway, HER2 is tied to HIF-1α and VEGF, which induces angiogenesis (Figure 3)[17]. HER2 gene amplification occurs in over 20% of human breast cancers[18]. HER2 amplification is associated with nodal metastasis[19], disease recurrence[20], and chemotherapeutic resistance. Patients with tumors showing HER2 gene amplification have shorter disease-free and overall survival[18].

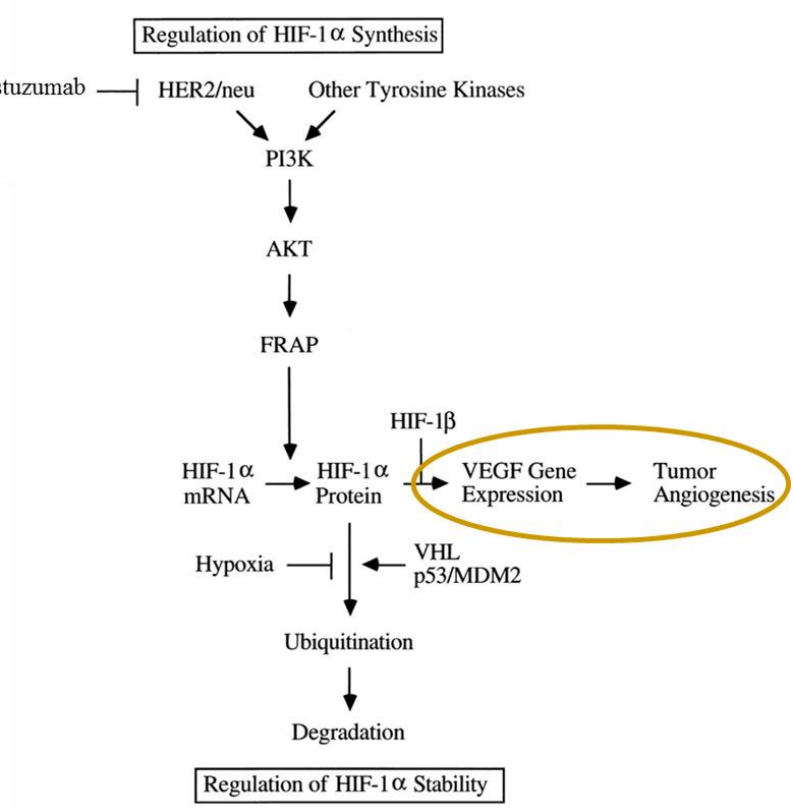

Figure 3: Trastuzumab affects tumor angiogenesis through the PI3K-AKT pathway. Blockage of HER2 by trastuzumab influences HIF-1α and VEGF expression. Modified from [17].

Trastuzumab Mechanism and Effect on Tumor Vasculature

Trastuzumab is a monoclonal antibody against the extracellular domain of HER2, and has been shown to be beneficial for patients with HER2 positive tumors when given in combination[21], or alone[22]. Trastuzumab binding prevents activation of the intracellular tyrosine kinase of HER2. Several mechanisms are hypothesized to reduce HER2 signaling, including inhibition of HER2 dimerization with other *erb*B receptors, increased degradation of HER2, and immune activation[23]. Trastuzumab has been tied to angiogenesis through both HIF-1α[17], and Heregulin pathways[16]. Trastuzumab has been shown to have anti-angiogenic effects

with immunohistochemical[9], and optical methods[24]. However, other immunohistolochemical studies have shown an increase in vascular content with trastuzumab treatment.

Optical Techniques for Quantification of Breast Tumor Angiogenesis

Optical Vascular Imaging Techniques

Non-invasive optical imaging methods are currently emerging that have the potential to augment or replace the traditional techniques for monitoring microvascular structure and oxygenation. Non-invasive methods are especially attractive for repeated measures, which are needed to study dynamic phenomena such as vascular growth and remodeling during ischemic recovery. Techniques like OCT[25]–[27], DOSI[28]–[30], photoacoustics[31], [32], and hyperspectral imaging[33]–[35], have been developed to image vascular morphology and blood oxygenation.

Microvascular oxygenation (sO_2) is a valuable endpoint in the study of angiogenesis pathology. Oxygenation is a measure of functional capability of the vascular system. Current methods to measure oxygenation in tissue include polarographic electrodes and fluorescence lifetime needle-based sensors, but both suffer from point-based sampling and invasiveness[36]. Non-invasive electron paramagnetic resonance oximetry is non-invasive, but requires exogenous contrast[37]. Endogenous contrast optical methods such as diffuse optical spectroscopy has been used to determine both oxygenation as well as lipid and water content in tissue, however only at low resolution[28]–[30].

Hyperspectral Imaging of Microvasculature

Hyperspectral imaging is a non-invasive optical technique that leverages the unique absorption spectra of oxygenated and deoxygenated blood to determine the blood oxygen concentration in tissue, using a modified version of Beer's Law[33]–[35]. Hyperspectral imaging

can obtain microvascular resolutions[33], and is compatible with longitudinal analysis[38]. Hyperspectral imaging has found application in preclinical tumor models[33], as well as clinical applications for diabetes[39], burn wounds[40], and hemorrhagic shock[41].

Hyperspectral imaging uses a white light source, a tunable band pass filter, and a camera to collect the raw data (Figure 4). Hyperspectral imaging calculates attenuation spectra per pixel, providing 3D data cubes with two spatial dimensions and one spectral dimension. In the visible light range, oxygenated and deoxygenated hemoglobin are dominant sources of tissue attenuation. Therefore, attenuation curves derived from hyperspectral images can be decomposed into relative contributions from both oxygenated and deoxygenated hemoglobin per pixel (Figure 5). These values can then be combined to derive 2D distribution maps of oxygenation.

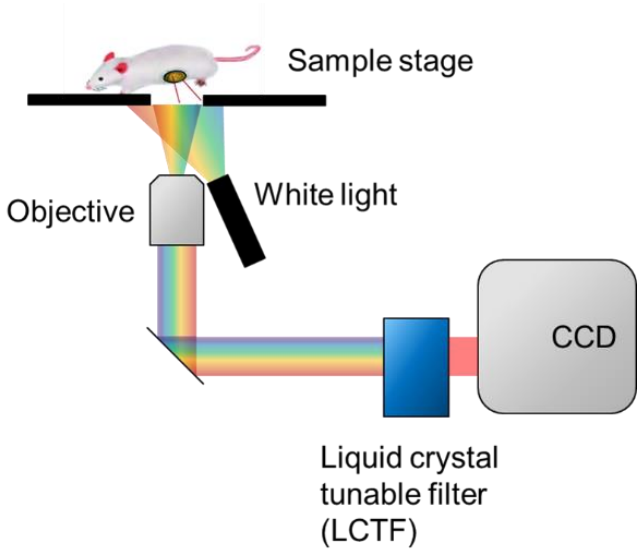

Figure 4: Hyperspectral Imaging Schematic. 4x objective collects light in an epi-illumination configuration. Resulting images are 2.11 x 1.58 mm with ~10 μm resolution.

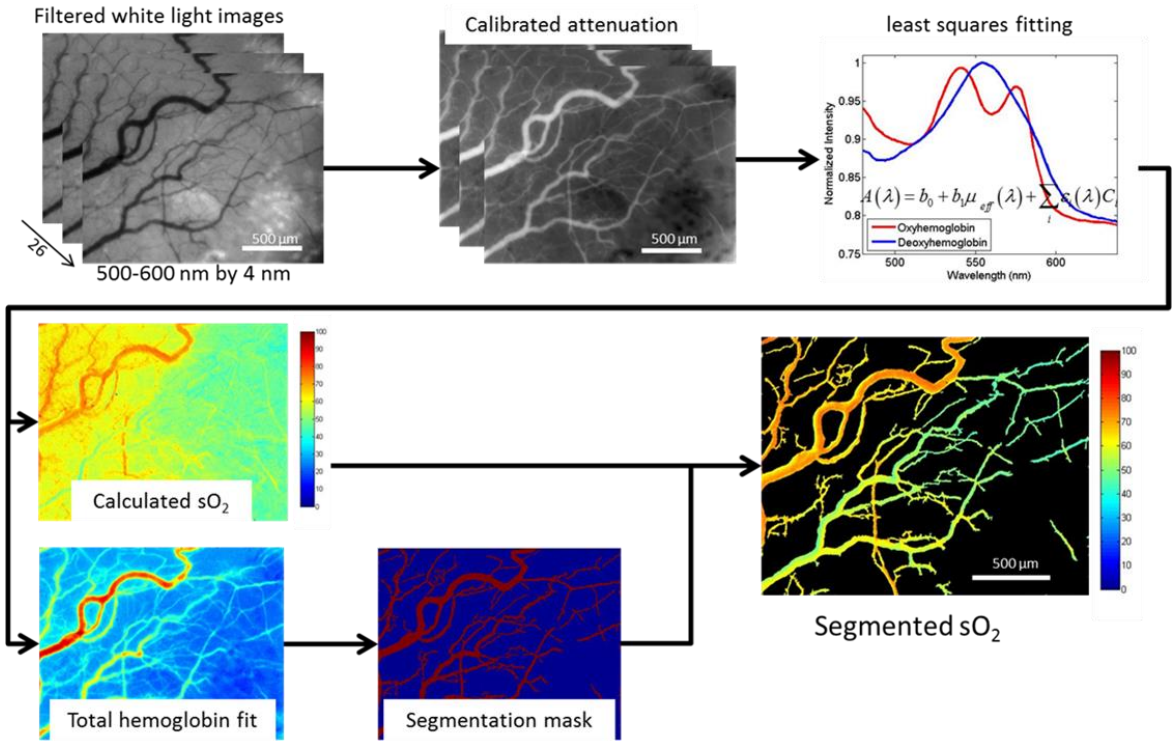

Figure 5: Hyperspectral Image processing to create sO¬2 maps. Blood oxygenation is calculated as a ratio of attenuation contribution of oxy- and deoxy-hemoglobin.

Quantification of Oxygen Saturation (sO_2)

Raw hyperspectral data cubes are processed through the spectral dimension. Measured intensity per-wavelength (I_{raw}) is calibrated with the corresponding dark image (I_{dark}) as defined by Eq. 1:

$$I_{cal} = \frac{(I_{raw} - I_{dark})}{t_{exposure}} \quad \text{(Eq. 1)}$$

Where I_{cal} is the calibrated image and $t_{exposure}$ is the exposure time.

Absolute attenuation (*A*) of light in the tissue is then calculated by Eq 2:

$$A = \log \frac{10^{OD} I_{cal\ ND}}{I_{cal\ tissue}}$$

(Eq. 2)

Where $I_{cal\ ND}$ is the calibrated light image taken with a ND filter, $I_{cal\ tissue}$ is the calibrated tissue image, and *OD* is the optical density of the ND filter used. This wavelength dependent attenuation ($A(\lambda)$) can be described as a linear combination of attenuation factors in the tissue. Using a modified Beer's law, the wavelength dependent attenuation of light can be expressed by Eq 3:

$$A(\lambda) = b_0 + b_1 \mu_{eff}(\lambda) + \sum_i \varepsilon_i(\lambda) C_i, \qquad \mu_{eff} = \sqrt{3\mu_a(\mu_a + \mu_s')}$$

(Eq. 3)

Where b_0 is a constant to account for spectral reflection and source intensity, μ_{eff} is the modeled effective attenuation of tissue due to non-hemoglobin absorption and scattering, and b_1 modulates the magnitude of the μ_{eff} term. The term $\varepsilon_i(\lambda)$ describes the extinction coefficient of the i^{th} absorber as a function of wavelength. For visible wavelength hyperspectral imaging of sO_2, oxygenated and deoxygenated hemoglobin are the only two terms. Linear non-negative least squares fitting is used to extract b_0, b_1, C_{oxyhb} and $C_{deoxyhb}$ per pixel. C_{oxyhb} and $C_{deoxyhb}$ are composite terms describing the concentration and pathlength of attenuated light by each absorber. The sO_2 is described by Eq 5, under the assumption that the pathlength of attenuated light is the same for both oxygenated and deoxygenated hemoglobin:

$$sO_2(\%) = \frac{C_{oxyhb}}{C_{deoxyhb} + C_{oxyhb}} \times 100$$

(Eq. 4)

Poorly fit pixels are rejected based on a goodness of fit parameter (R^2 value) defined by Eq. 5:

$$R^2 = 1 - \frac{SS_e}{S_t}, \qquad R^2 < 0.9 \tag{Eq. 5}$$

Where SS_e is the error sum of squares and S_t is the total variance, however most pixels will have a R^2 greater than this. The sO_2 values are then displayed on a pseudo-colored scale ranging between 0% (deoxygenated) and 100% (fully oxygenated).

CHAPTER 2

IN VIVO HYPERSPECTRAL IMAGING OF MICROVESSEL RESPONSE TO TRASTUZUMAB TREATMENT IN BREAST CANCER XENOGRAFTS

Introduction

In 2013, more than 200,000 new cases of breast cancer were diagnosed, with breast cancers accounting for more than 40,000 deaths in the United States[42]. The HER2 gene is amplified in approximately 20% of breast cancers. Overexpression of HER2 is predictive of poor patient outcome[15], [18]. Trastuzumab, a humanized monoclonal antibody specific to HER2, improves survival in patients with HER2-amplified breast cancers[22], [43]. Although several mechanisms of action contribute to the clinical success of trastuzumab, one mechanism involves trastuzumab-mediated inhibition of HER2 signaling pathways that control tumor cell proliferation and survival. Because HER2 signaling induces expression of the angiogenic factor vascular endothelial growth factor (VEGF), HER2 inhibition dampens VEGF production, thus normalizing tumor vasculature[24]. Normalized vasculature improves drug, oxygen, and nutrient delivery in tumors[14], thereby improving tumor response to chemotherapy and radiation therapy[44]. Therefore, HER2 inhibition has the dual effect of inhibiting tumor cell growth and normalizing tumor vasculature for improved treatment response. However, as many as one-third of HER2 overexpressing tumors do not initially respond to trastuzumab [45]. Further, HER2 positive tumors have been shown to acquire resistance to Trastuzumab over time[23]. The effect of trastuzumab resistance on tumor vasculature remains poorly understood.

Immunohistochemistry, the gold standard technique for assessment of tumor vasculature, has shown that treatment with trastuzumab decreases tumor VEGF and CD31 (a vascular

endothelial marker) content in HER2-amplified xenografts after 28 days[9]. Interestingly, other studies performed at earlier time points (14 days) after trastuzumab treatment demonstrated increased CD31[8]. Although these studies identified seemingly disparate findings, it is possible that trastuzumab causes dynamic changes in the tumor vasculature that change with time. Capturing dynamic vascular responses to trastuzumab would require longitudinal measurements of vascular structure and function *in vivo*.

The most common methods for longitudinal imaging of tumors include PET[10] and CT[11], which require injected contrast; and MRI, which can measure both tumor size[12], [46] and tumor vasculature [13]. However, none of these techniques have sufficient resolution to image microvasculature. An optical based technology, Diffuse Optical Spectroscopic Imaging (DOSI), is sensitive to changes in blood oxygenation, bulk vascularization, water content, and fat content in primary breast tumors within a week of treatment with the chemotherapeutics doxorubicin and cyclophosphamide [28]. DOSI has also shown that oxygenated and deoxygenated hemoglobin content are predictive of response to doxorubicin and cyclophosphamide within one week of the start of chemotherapy[29]. However, DOSI measurements are inherently low resolution and therefore cannot resolve the dynamic behavior of the microvasculature.

To achieve high resolution imaging of tumor microvasculature, we used hyperspectral imaging, an optical imaging technique that resolves blood oxygenation and vascular density at microvascular resolution, with higher resolution than PET, CT and MRI, and DOSI. Hyperspectral imaging is useful as a non-invasive, high resolution tool to image tumor hypoxia[33], [35]. Importantly, hyperspectral imaging is compatible with longitudinal analysis[38], making this an ideal technique for assessing changes in the tumor microvasculature over time. Hyperspectral imaging uses band-pass filtered white light to quantify the relative amounts of oxygenated and

deoxygenated hemoglobin in microvessels, thereby creating blood oxygen saturation (sO_2) maps of microvasculature[47]. Segmentation of microvessels within hyperspectral images also allows for quantification of structural endpoints including vessel density and branching[48], [49]. Therefore, these strengths of hyperspectral imaging make it advantageous for quantifying the *in vivo* tumor microvascular response to anti-cancer treatment over an extended time-course.

We used hyperspectral imaging to quantify the microvascular response to trastuzumab treatment in both trastuzumab-responsive and trastuzumab-resistant breast tumors in real time. Results showed that trastuzumab increased microvessel density in trastuzumab-responsive tumors at 5 and 14 days post-treatment, but not in trastuzumab-resistant tumors at either time point. Conversely, sO_2 was decreased in both trastuzumab-responsive and -resistant tumors at 5 days post-treatment. Importantly, responsive tumors showed significantly higher vessel density and significantly lower sO_2 than all other groups at 5 days post-treatment. These studies demonstrate the utility of hyperspectral imaging as a non-invasive approach to measure changes in tumor microvasculature as a function of therapeutic response.

Materials and methods

Tumor Model

This study was approved by the Vanderbilt University Institutional Animal Care and Use Committee and meets the National Institute of Health guidelines for animal welfare. BT474 (trastuzumab-responsive) and HR6 (trastuzumab-resistant)[50], human breast cancer cell lines were used in all experiments. Both cell lines overexpress HER2, however HR6 are resistant to trastuzumab treatment. HR6 cells were derived from parental BT474 xenografts that grew exponentially despite continuous treatment with trastuzumab [50]. Nude mice were injected with 10^7 cancer cells (either BT474 or HR6) in Matrigel into the right mammary fat pad. After 10 days,

when the tumors were ≥ 150 mm^3, a mammary window was surgically implanted over the tumor area. Mice were randomized to receive twice weekly treatment with trastuzumab 10 mg/kg i.p. (Vanderbilt Outpatient Pharmacy) or a control antibody (human IgG_1 10 mg/kg i.p., R&D Systems) for 14 days. Tumor vasculature was imaged on days 2, 5, 9, and 14 after initial treatment, through the mammary window. Tumor volume was measured every other day in a matching cohort of mice, using caliper measurements of tumor length (L) and width (W), with total tumor volume calculated as $(LxW^2)/2$.

Immunohistochemistry

A separate cohort of nude mice was used to generate histological tumor sections over the time-course. Tumors were grown and treated as above, however no mammary windows were implanted. Tumors were harvested on treatment days 2, 5, and 14, formalin fixed and paraffin embedded. Sections (5-µm) were used for immunohistochemistry staining and quantification (n = 3 per time point per condition).

Ki67 (a marker of proliferation) and cleaved caspase-3 (CC-3, a marker of apoptosis) immunohistochemistry (IHC) was performed by the Vanderbilt Translational Pathology Shared Resource using diaminobezidine (DAB) contrast. For VEGF and CD31 IHC, slides were de-paraffinized, rehydrated, subjected to heat mediated antigen retrieval in sodium citrate buffer at 95-100°C for 40 min, incubated in 3% H_2O_2 for 10 min, blocked in 10% donkey serum overnight at 4°C, incubated in primary antibody overnight at 4°C [rabbit VEGF (1:50) or rabbit CD31 antibody (1:100; both from Santa Cruz Biotechnology), washed and developed with Vectastain ABC kit (Vector Labs, for VEGF staining), or stained with secondary FITC conjugated goat anti-rabbit antibody (1:100, Invitrogen), washed and counterstained with Prolong Gold Anti-Fade with DAPI.

Histological Analysis

Quantification of Ki-67, CC-3, and VEGF staining was performed by counting the number of positive cells and the total number of tumor cells within 5 fields of view from three tumors per group (~30-100 cells per image). The reported value is the percentage of cells that are positive for any of the markers.

CD31 slides were surveyed using fluorescence microscopy to find three areas of maximum expression. Images were taken on a fluorescence microscope using a 10X objective with a FITC filter to obtain images of CD31 staining, and a DAPI filter to obtain images of nuclear staining. DAPI staining was used to outline viable, non-necrotic tumor tissue and CD31 was quantified as total CD31 pixels over total non-necrotic tumor area.

Animal Handling for Imaging

For *in vivo* imaging, mice were anesthetized using 1.5% isoflurane in air and maintained at normal body temperature using a circulating water heating pad. Mice were placed over the microscope objective with the window chamber lightly positioned and stabilized on a custom support device centered over the objective. After imaging, mice were allowed to fully recover from anesthesia before returning them to their cage.

Hyperspectral Imaging

After window implantation, mice were imaged using a custom built hyperspectral system attached to an inverted microscope (TiE, Nikon). Hyperspectral hardware was controlled with custom Labview software to acquire filtered white light data cubes. White light from a halogen light source was directed through a liquid light guide to illuminate the mammary window chamber in an epi-illumination configuration. Back-scattered light was collected through a 4x air objective,

passed through a narrow band-pass liquid crystal tunable filter (Cambridge Research and Instrumentation, Varispec VIS), and onto a -20°C cooled CCD camera (Andor, Clara). The filter was automatically adjusted from 500 nm to 600 nm by 4 nm increments, and images were acquired for 500 ms at each wavelength resulting in a 1040x1392x26 pixel data cube of back reflected intensity. Daily lamp spectrum and dark offset measurements were collected to eliminate day-to-day variability and to calibrate the spectra. Data cubes were processed with custom MATLAB code to calculate absolute attenuation of light per wavelength. Non-negative least squares fitting was used to fit absolute attenuation to a modified version of Beer's law; extracting relative contribution of tissue, oxygenated hemoglobin, and deoxygenated hemoglobin to the total attenuation at each pixel[35]. Four acquisitions were taken in each mouse, over visibly vascularized areas of the tumor. Care was taken to image the same region of the tumor over the time course, based on vascular morphology. Each field of view was 1.58 x 2.11 mm with ~10 μm lateral resolution. Additional MATLAB post processing code derived quantitative values including blood oxygen saturation (oxygenated hemoglobin/total hemoglobin, sO_2), total relative hemoglobin per pixel (oxygenated hemoglobin + deoxygenated hemoglobin), vessel density (positive vessel area/total image area), vessel branch points (points where vessels branch into multiple vessels), vessel diameters (average perpendicular distance to vessel segment length), vessel lengths (sum of skeletonized vessel), and tortuosity (vessel length/straight line distance).

Image Quantification

Images were segmented using the high contrast, total relative hemoglobin images. A Gabor filter was used to segment vessel-like features[51]. Briefly, a Gabor filter is a cosinusoidal modulated Gaussian, which acts as a directional low-pass filter. A Gabor kernel was generated for angles between 0 and π and convolved with the total hemoglobin image. For each pixel, the maximum value of the convolution was saved in a maximum value image. The Gabor kernel size was then varied through the entire range of vessel sizes in the image (20 to 300 μm), and a final mask was generated as a sum of the maximum value images for all kernel sizes. A logical mask was created by thresholding to select maximum value pixels greater than 0.5 (range from 0-1), which removed background noise from the pixel mask. Vessel density was computed as the sum of pixel values of the logical mask divided by the total number of pixels in the image. Blood oxygen saturation percent (sO_2) was computed as the mean sO_2 value of all masked pixels within an image. Each image was manually screened for segmentation integrity and fitting to hemoglobin curves. Poorly segmented or ill fit (R^2 threshold < 0.9) images were excluded from analysis.

For distribution analysis of individual microvessel sO_2, vessel maps were skeletonized[48] and vessel branch points were determined as the intersection of skeletonized vessels. Using branch points, vessel segments were isolated, and mean sO_2 was calculated per vessel segment. Histograms were created using all vessel segment sO_2 values in a group at each time-point. One or two Gaussians were optimally fit to each histogram (using Expectation Maximization[52] and selecting minimal Akaike Information Criterion or AIC[53]). Histograms that were optimally fit to two Gaussians were split into two groups using Expectation Maximization[52]. Higher oxygenated vessels were collected into an “arterial” group while lower oxygenated vessels were

collected into a "venous" group for ease of reference. Mean and standard error of the mean (SEM) was taken from the expectation maximization algorithm for the "arterial" and "venous" groups. Total probability of vessel segments belonging to either "arterial" or "venous" group was not quantified, but expressed as the relative area under the curve of each Gaussian in the histogram.

Statistics

Statistical significance was determined using two-sided Student's *t* tests. P values <0.05 were considered statistically significant. Values are expressed as mean ± SEM. N was determined as the number of properly fitted and segmented images in a group.

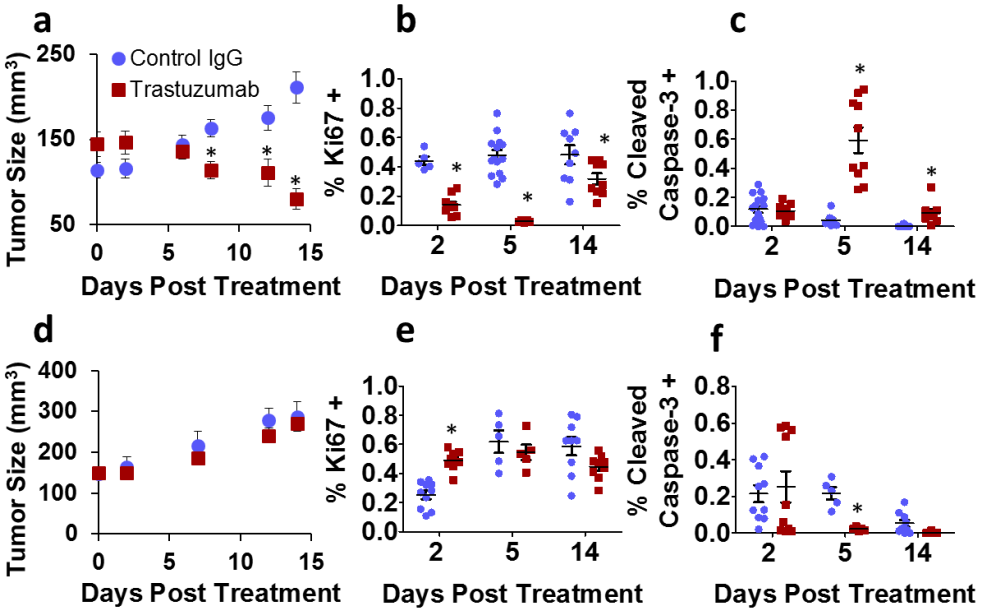

Figure 6: Tumor response in trastuzumab-responsive (a-c) and –resistant (d-f) xenografts treated with control IgG and trastuzumab. BT474 (trastuzumab-responsive) tumor growth curves (a). Percent of cells positive for Ki67 (% Ki67+), in BT474 tumors (b), and percent of cells positive for CC-3 (% cleaved caspase-3 +), in BT474 tumors (c) at days 2, 5, and 14 post treatment. HR6 (trastuzumab-resistant) tumor growth curves (d). Ki67 immunohistochemistry in HR6 tumors

(e), and CC-3 immunohistochemistry in HR6 tumors (f) at days 2, 5, and 14 post treatment. Asterisks (*) indicate $p<0.05$ between control IgG and trastuzumab treated groups. Bar indicates mean with SEM error bars.

Results

Histology Confirms BT474 Sensitivity and HR6 Resistance to Trastuzumab Treatment

To examine the impact of trastuzumab on tumor microvasculature *in vivo*, we transplanted BT474 human HER2-amplified breast cancer cells into athymic nude mice. Previous studies demonstrate that BT474 cells are highly sensitive to trastuzumab. We also used HR6 cells, a sub-line of BT474 selected *in vivo* for acquired resistance to trastuzumab. By day 8, trastuzumab-treated BT474 tumors showed a significant decrease in tumor size compared with tumors treated with IgG by day 8; this effect persisted through day 14 (Figure 6a). The percent of cells positive for Ki-67 was significantly lower in trastuzumab-treated BT474 compared to controls for all treatment time-points (2, 5, and 14 days, Figure 6b). The percent of cells positive for CC-3 (an immunostain for apoptosis) was significantly higher in trastuzumab-treated tumors versus those treated with IgG (Figure 6c). In contrast, HR6 tumors treated with trastuzumab did not show any significant differences in tumor size over 14 days of treatment (Figure 6d), had significantly higher proliferation (Ki67) than controls on day 2 but not at later time points (Figure 6e), and exhibited decreased apoptosis on day 5 as compared to tumors treated with IgG. Comparison of IgG-treated controls showed that HR6 xenografts exhibited faster tumor growth after day 7, increased proliferation on days 2 and 5, and increased apoptosis on days 5 and 14 over IgG-treated BT474 drug-sensitive xenografts. A comparison of trastuzumab-treated groups shows that BT474 tumors have significantly reduced tumor growth after day 3, increased proliferation at all time-points, and increased apoptosis on days 5 and 14 compared to HR6 tumors ($p<0.05$).

To determine the impact of trastuzumab treatment on expression of the angiogenic factor VEGF, we performed VEGF immunohistochemistry on histological tumor sections. Decreased VEGF expression was seen in trastuzumab-treated BT474 tumors on days 2 and 5 (Figure 7a). Trastuzumab-treated HR6 tumors also showed significantly lower VEGF (Figure 7b) on day 5. In contrast to these results, IHC for CD31, a molecular marker of vessel endothelial cells, revealed increased vessel density in trastuzumab-treated BT474 tumors on day 2 (Figure 7c) but no significance difference in vessel density in trastuzumab-treated HR6 tumors as compared to IgG-treated controls Figure 7d). Under basal conditions, VEGF expression was similar in BT474 and HR6 tumors, although HR6 tumors had significantly higher CD31 staining than BT474 tumors on day 2. A comparison of trastuzumab-treated groups shows that BT474 tumors had significantly reduced VEGF on days 2 and 5, and reduced CD31 on day 5 versus HR6 tumors ($p<0.05$).

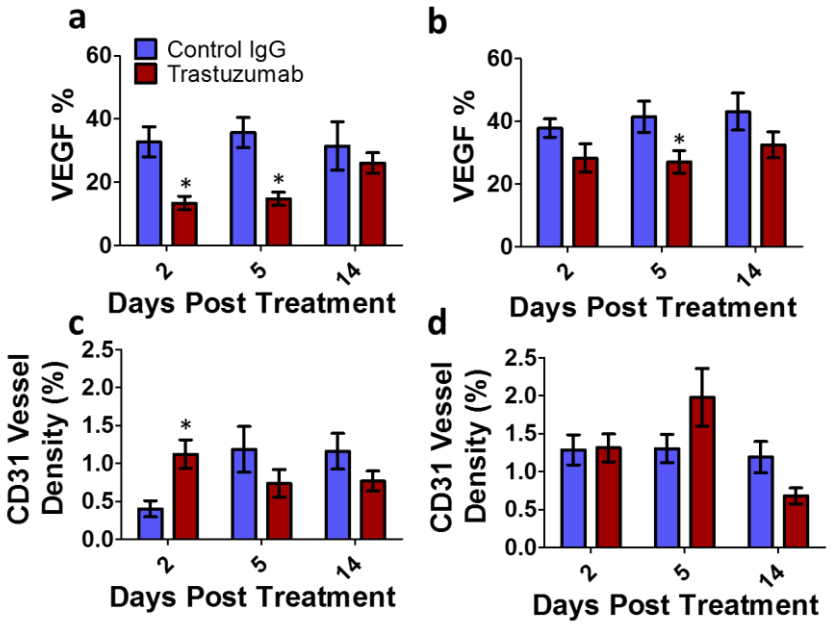

Figure 7: Immunohistochemistry of BT474 (a, c) and HR6 (b, d) tumor xenografts. (a, b) VEGF area percentage (number of high expression tumor cells divided by total number of tumor cells) for control IgG and trastuzumab-treated tumors at 2, 5, and 14 days after initial treatment in trastuzumab-responsive BT474 tumors (a) and trastuzumab-resistant HR6 tumors (b). (c, d) CD31 vessel density (number of high expression pixels divided by total number of non-necrotic tumor pixels) in BT474 (c) and HR6 (d) tumors. Bars indicate mean and SEM of data. Asterisks (*) indicate $p<0.05$ between control IgG and trastuzumab treated groups.

Hyperspectral Imaging Reveals Dynamic Changes in Tumor Microvasculature of Trastuzumab-Treated Tumors

Hyperspectral images were used to assess BT474 and HR6 tumors treated with trastuzumab or IgG on days 2, 5, 9, and 14. Representative segmented images for the time-course are shown in **Error! Reference source not found.**. Qualitatively, visual changes in vascular diameter and ortuosity were observed over the time-course, with an accompanying decrease in microvessel sO_2 in all groups at later time-points. Quantitative analysis is shown in Figure 9. Trastuzumab-treated BT474 tumors showed a significant decrease in microvessel sO_2 on day 5 (Figure 9a), as well as significant increases in vessel density on days 5 and 14 (Figure 9c) compared to IgG-treated

controls. Additionally, trastuzumab-treated HR6 tumors showed a significant decrease in microvessel sO_2 on day 5 versus controls (Figure 9b). However there was no significant difference in vessel density between trastuzumab-treated and IgG-treated controls during the time-course (Figure 9d). Furthermore, trastuzumab-treated tumors (both BT474 and HR6) had significantly lower microvessel sO_2 values on day 5 compared to day 2, whereas IgG-treated tumors (both BT474 and HR6) had significantly lower microvessel sO_2 values at a later time-point (day 9) compared to day 2 (Figure 9a-b). These decreases in microvessel sO_2 were sustained through day 14 post-treatment (Figure 9a-b). Comparison of control IgG groups showed no significant difference in sO_2 or vessel density between HR6 control IgG and BT474 control IgG xenografts. A comparison of trastuzumab-treated groups showed that BT474 tumors had significantly lower sO_2 and higher vessel density on day 5 versus HR6 tumors ($p<0.05$). Other quantified endpoints such as vessel branch points, vessel diameters, vessel lengths, and tortuosity did not show significant differences between the groups.

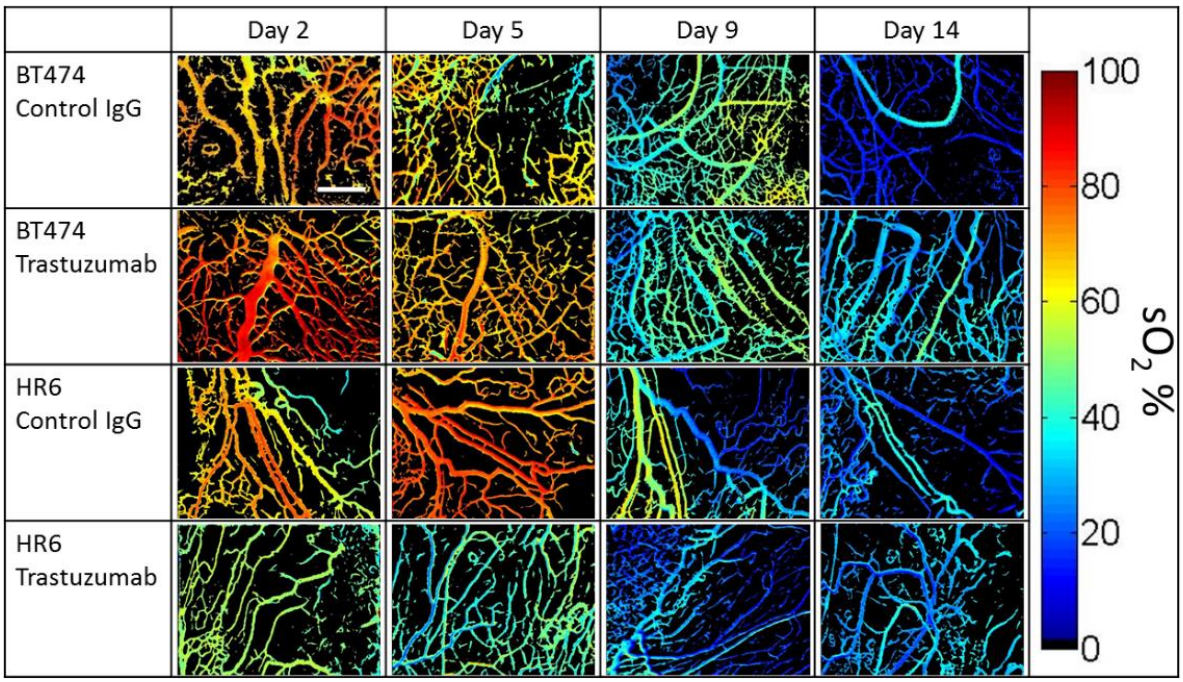

Figure 8: Representative in vivo hyperspectral time-courses for a single mouse in each treatment group. Colormap indicates sO_2 percentage, from 0% (dark blue) to 100% (dark red). Non-vascular tissue is segmented out and indicated by black background. Changes in microvascular morphology and sO_2 are seen in all treatment groups. Scale bar (500 microns) is in BT474 Control IgG, Day 2 image.

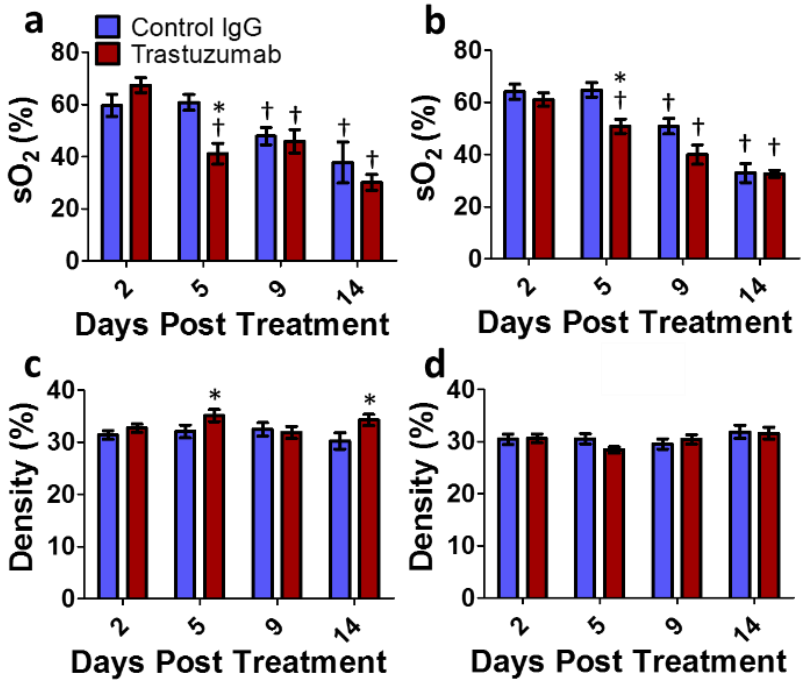

Figure 9: Oxygen saturation (sO2) and vessel densities derived from in vivo hyperspectral time-course. Average vessel sO_2 for control IgG and trastuzumab-treated (a) BT474 and (b) HR6 tumors imaged 2, 5, 9, and 14 days after initial treatment. Percent vessel density (vessel area divided by total area) calculated from BT474 (c) and HR6 (d) xenografts. Bars indicate mean and SEM of all images acquired in each group. Asterisks (*) indicate $p<0.05$ between control IgG and trastuzumab treated groups. Daggers (†) indicate $p<0.05$ versus day 2 in the same group.

Analysis of sO_2 Distribution Emphasizes Microvascular Shift Towards Lower sO_2 Over Time-course

We next used hyperspectral imaging to assess treatment-induced changes in sO_2 distribution in the microvasculature of BT474 and HR6 tumors. Microvessel segments were separated by branch point, gathered into histograms of mean microvessel segment sO_2, and optimally fit to one or two Gaussians. Figure 10a shows a representative histogram and two-Gaussian fit for the sO_2 of microvessel segments in IgG-treated BT474 xenografts on day 2 post-treatment. Distributions that lent themselves to two-component Gaussian fits were further categorized into two groups by sO_2 level; the higher sO_2 Gaussian described highly oxygenated "arterial" vessels while the lower sO_2 Gaussian described poorly oxygenated "venous" vessels. Figure 10b-e shows the evolution of the Gaussian fits over the time-course. trastuzumab-treated BT474 tumors (Figure 10c) showed a large shift in high oxygenated "arterial" contributions towards more deoxygenated (lower) sO_2 levels, while the highly oxygenated contribution in IgG-treated tumors (Figure 10b) did not shift more than 5% from an sO_2 value of ~55%.

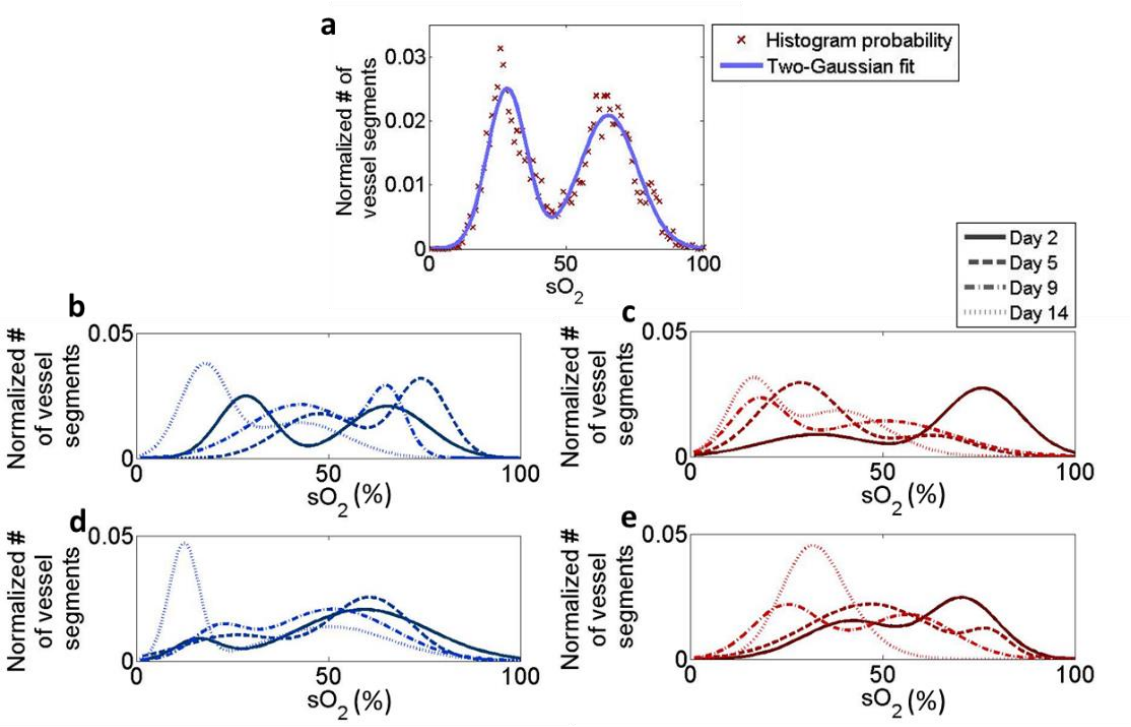

Figure 10: Distribution analysis of microvessel segment sO_2. (a) Representative histogram and two-Gaussian fit for the sO_2 of microvessel segments in BT474 control tumors on day 2 post-treatment. Red x's indicate histogram probability value, blue curve indicates optimum fit. Changes in the distributions over the time-course (days 2, 5, 9, and 14 post-treatment) for (b) control IgG, and (c) trastuzumab-treated BT474 tumors. Changes in the distributions over the time-course (days 2, 5, 9, and 14 post-treatment) for (d) control IgG, and (e) trastuzumab-treated HR6 tumors.

Distributions that were bimodal were further quantified as the mean and SEM of the two modes. The distribution of trastuzumab-treated HR6 tumors on day 14 is the only distribution that was optimally fit to a single Gaussian (Figure 10e); further quantification uses the mean and standard deviation of the single Gaussian for the "venous" group, with no contribution from an "arterial" group for that time-point. IgG-treated BT474 tumors showed no significant changes in arterial or venous component means over the time-course (Figure 11a,c), while the "arterial" and "venous" components of trastuzumab-treated BT474 xenografts exhibited significantly lower sO_2 on day 14 compared to day 2 (Figure 11a, c). The trastuzumab-treated "arterial" component of

BT474 tumors was significantly higher than control IgG on day 2, and significantly lower than control on day 14 (Figure 11a). The trastuzumab-treated HR6 "arterial" component was significantly higher on day 5, and lower on day 9 compared to control IgG (Figure 11b). The trastuzumab-treated HR6 "venous" component was significantly higher on day 2 and 14, and significantly lower on day 9 compared to control IgG (Figure 11d). A comparison of control IgG groups showed that IgG-treated BT474 xenografts had significantly lower arterial sO_2 on days 5 and 9, and lower venous sO_2 on days 2, 5, and 9 when compared to control IgG-treated HR6 xenografts ($p<0.05$). A comparison of trastuzumab-treated groups shows that BT474 tumors have significantly lower "arterial" sO_2 on day 5, and lower "venous" sO_2 at all time-points ($p<0.05$).

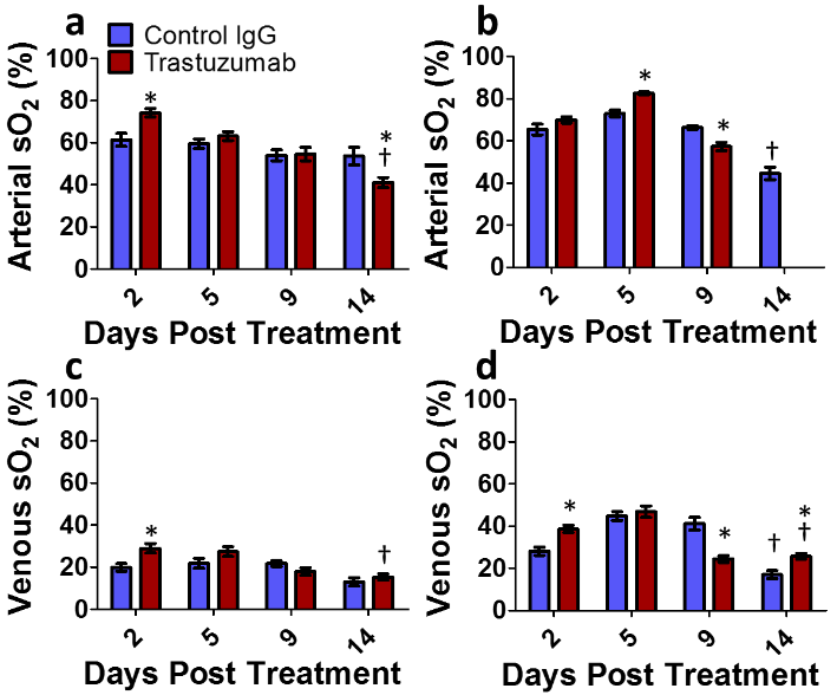

Figure 11: Vessel segment sO2 values of "arterial" and "venous" contributions over the treatment time-course. The sO_2 of the arterial component from (a) BT474, and (b) HR6 tumors on days 2, 5, 9, and 14 after initial treatment. sO_2 of venous component from (c) BT474 and (d) HR6 tumors. Asterisks (*) indicate $p<0.05$ between control IgG and trastuzumab-treated groups. Daggers (†) indicate $p<0.05$ versus day 2 in the same group. Bars represent mean ± SEM.

Table 1. Time-points at which significant changes in histological and hyperspectral endpoints were measured with trastuzumab treatment in BT474 and HR6 xenografts

	Histological endpoints				Hyperspectral endpoints			
Quantified measures	Ki67 (days)	CC-3 (days)	VEGF (days)	CD31 (days)	Vessel density (days)	Total sO_2 (days)	Arterial sO_2 (days)	Venous sO_2 (days)
BT474 trastuzumab vs. control IgG	2, 5, 14	5, 14	2, 5	2	5, 14	5	2, 14	2
HR6 trastuzumab vs. control IgG	2	5	5	*n.s.*	*n.s.*	5	5, 9	2, 9, 14

Number indicates time-point (days) at which the trastuzumab-treated group is significantly different than control IgG ($p<0.05$)
n.s. indicates no significant difference between trastuzumab-treated and control IgG ($p>0.05$)

Discussion

Little is known regarding how trastuzumab impacts the tumor microvasculature, per se, due to limitations in imaging resolution, dynamic changes in microvasculature over time, and innate differences in the tumor microvasculature of trastuzumab-resistant versus trastuzumab-sensitive HER2-amplified breast cancers. In this study we quantified tumor cell and vascular response to trastuzumab treatment in trastuzumab-responsive BT474 tumors and trastuzumab-resistant HR6 tumors over a 14 day time-course. Table 1 displays the histological and hyperspectral endpoints investigated in this paper, and the time-points at which significant differences were measured between control IgG and trastuzumab-treated groups. trastuzumab decreased tumor volume and proliferation (Ki67), and increased apoptosis (CC-3) in BT474 tumors, consistent with previously published reports[8], [54]. In contrast, trastuzumab did not

inhibit tumor growth, proliferation, or cell survival in HR6 tumors, also consistent with previous findings[50].

VEGF is highly expressed in many tumors in an effort to vascularize a rapidly growing cell mass[55], [56]. Immunohistochemistry in BT474 tumors (Figure 7a, c) showed that trastuzumab treatment reduced VEGF expression compared to control IgG on days 2 and 5 post-treatment, in agreement with previous studies [8], [9]. These previous studies also showed increased CD31+ vessel density in trastuzumab treated BT474 tumors at 14 days post-treatment[8], consistent with our results showing increased CD31+ vessel density in trastuzumab-treated compared BT474 tumors at day 2. However, VEGF expression was decreased in trastuzumab-treated BT474 tumors on day 2. This inverse relationship between VEGF expression and CD31 vessel density on day 2 highlights the complex connection between growth factor expression and angiogenesis[2], and indicates that angiogenic factors other than VEGF may drive vascular proliferation in trastuzumab-treated BT474 tumors. Tumor size, proliferation, apoptosis, and VEGF expression in the BT474 tumors support the hypothesis that trastuzumab treatment reduces tumor mass and VEGF expression in drug-sensitive, HER2-dependent tumors. The higher CD31 content on day 2 for trastuzumab treated vs. IgG-treated BT474 tumors suggests that the effect of the antibody on tumor size initially outpaces vessel pruning, thus increasing vessel density by reducing tumor bulk.

Trastuzumab did not inhibit cell proliferation or cell death in HR6 tumors, so we predicted that trastuzumab treatment would have no significant effect on HR6 tumor cells or the supporting tumor vasculature. However, we did see a significant decrease in VEGF expression 5 days after initial trastuzumab treatment, suggesting that HER2 signaling may still influence VEGF expression levels in these resistant tumors. Regardless, decreased VEGF levels in trastuzumab-

treated HR6 tumors did not manifest as a significant change in CD31 vessel density at any time point, supporting the notion that many mechanisms contribute to therapeutic resistance to trastuzumab, including the ability of tumor cells to support tumor vasculature. In fact, one primary mechanism of trastuzumab resistance in HR6 tumors is through upregulation of heregulin, a known pro-angiogenic factor, which may be able to compensate for decreased VEGF production in the presence of trastuzumab[50]. Importantly, a comparison of trastuzumab-treated groups identified a clear difference in microvessel density of trastuzumab-responsive and trastuzumab-resistant tumors that was measurable using hyperspectral imaging.

Hyperspectral imaging of sO_2 (Figure 9a-b) illustrates an overall decrease in microvessel sO_2 over the time-course for all groups. This agrees with the DOSI-measured decrease in sO_2 in tumors one week after initiation of therapy[29]. Additionally, BT474 tumors exhibited a significant decrease in sO_2 with treatment compared to all other groups on day 5. This decrease in sO_2 with trastuzumab treatment in BT474 tumors provides insight into other *in vivo* cellular metabolic imaging studies performed by our laboratory [57]. Our previous study showed a decrease in aerobic metabolism in BT474 tumors 5 days after initial trastuzumab treatment compared to control IgG, which is in agreement with the decreased microvessel sO_2 seen on day 5 in the current study.

Hyperspectral imaging measured an increase in microvessel density in trastuzumab-treated BT474 xenografts compared to all other tumors (Figure 9c), which agrees with CD31-measured increases in microvessel density (Figure 7c). These results are also consistent with previous studies that showed that CD31 vessel density increased 14 days after initial treatment[8]. Note that our CD31 histology shows an increase in vessel density 2 days after treatment of mice bearing BT474 tumors, but hyperspectral imaging of vessel density does not detect a significant

increase until day 5. This may be due to the higher resolution of histological analysis (~5 μm compared to ~20 μm for these hyperspectral experiments), and an abundance of endothelial growth in these tumors that does not form functional vessels and exhibits later vessel regression[2]. These non-perfused vessels are not quantified in hyperspectral measures of vessel density that rely on hemoglobin for contrast, but are still detectable by CD31 IHC.

For trastuzumab-resistant HR6 tumors, we hypothesized that there would be no vascular effect due to trastuzumab treatment over the time-course. However, hyperspectral imaging showed a significant decrease in microvessel sO_2 in trastuzumab-treated HR6 tumors 5 days after initial treatment. This may indicate that there was a secondary effect of trastuzumab on host stromal cells as hypothesized by other groups[24], even though trastuzumab treatment did not result in overall tumor shrinkage. Importantly, trastuzumab-treated HR6 tumors had significantly lower vessel density than trastuzumab-treated BT474 tumors.

Distribution analysis highlighted the temporal changes in the sO_2 of highly oxygenated and low oxygenated microvessel compartments (Figure 10, Figure 11). The mean sO_2 of highly oxygenated "arterial" microvessels in trastuzumab-treated BT474 tumors decreased over the 14-day time-course (Figure 11a). This result agrees with published DOSI data that shows that responsive tumors have decreased oxygenated hemoglobin concentration 7 days after initial treatment with doxorubicin and cyclophosphamide[28]. In contrast, the "arterial" contribution of control IgG BT474 tumors was constant over the time-course (Figure 11a). The mean sO_2 of the "venous" microvessels in BT474 tumors also decreased with trastuzumab-treatment, while the control IgG group showed no change over the time-course.

In trastuzumab-resistant HR6 tumors, treatment with the antibody resulted in a single Gaussian distribution of microvessel sO_2 at 14 days (Figure 10e). This suggests that the

microvessels of trastuzumab-treated HR6 tumors all shifted to hypoxic levels at this time-point, and showed little differentiation into "arterial" and "venous" compartments suggestive of very abnormal vasculature[14]. Additionally, vessel distributions of trastuzumab-treated HR6 tumors were significantly different from trastuzumab-treated BT474 tumors. Trastuzumab-treated BT474 tumors had significantly lower "venous" contribution at all time-points, which also suggests a mechanistic difference between responsive and resistant groups starting 2 days post-treatment.

The heterogeneity of cancer and the dynamic nature of tumor microvasculature requires significant effort to unravel the relationships between dynamic changes in vascular growth factors, microvessel structure and sO_2, cell metabolism, and anti-cancer drug response. Using hyperspectral imaging, we quantified microvessel sO_2 and density over a time-course of trastuzumab treatment in both drug-responsive and -resistant tumors. These studies captured day-to-day changes in functional endpoints that are difficult to capture with single static metrics such as IHC and histology. Our conclusions with hyperspectral imaging endpoints were corroborated with histological data, and provided insight into the microvascular changes with anti-cancer treatment that contribute to changes in bulk tissue diffuse optical imaging endpoints. This work also provides insight into tumor oxygen supply that complements our previous work that imaged tumor oxygen demand (metabolism) *in vivo* in the same animal models and treatment[57]. Overall, these results quantified dynamic changes in microvascular structure and function, and suggests that longitudinal imaging of microvessel endpoints could distinguish trastuzumab-responsive from trastuzumab-resistant tumors, a finding that could be exploited in the post-neoadjuvant setting to guide post-surgical treatment decisions.

CHAPTER 3

CONCLUSIONS AND FUTURE DIRECTIONS

Immunohistochemistry is the gold standard of microvascular quantification in preclinical drug assessment. However, using *ex vivo* techniques to acquire longitudinal quantification is challenging. Preclinical imaging techniques such as PET, CT, MRI, and DOSI can track tumor progression longitudinally, however none achieve microvascular resolution. Hyperspectral imaging is a non-invasive technique that can perform morphological and functional measurements at high resolution. This study uses the advantages of hyperspectral imaging to quantify microvascular dynamics in an orthotopic mouse xenograft model. Vascular density and sO_2 was quantified over a 14 day time-course. Gold standard IHC and tumor size progression was also measured over a 14 day time-course. The results show decreased sO_2 and increased vessel density 5 days after treatment in sensitive tumors. Similarly, there was a decrease in sO_2 in resistant tumors 5 days after treatment, but no significant changes in vessel density parameters over the time-course were seen. The results shown indicate a vascular independent route of resistance in the HR6 tumor line.

Future work will include blood flow quantification to predict arteriogenic expansion of vessels. Flow phantom and ear punch experiments will validate Doppler OCT techniques. These measurements will be combined with already validated hyperspectral techniques to develop a complete vascular quantification toolbox. The toolbox will be applied to quantify the effect of direct vascular treatment using bevacizumab (anti-VEGF treatment) in a dorsal window chamber. This experiment will be designed to show the predictive value of flow and oxygenation on vascular morphology and tumor progression.

The interaction between blood flow dynamics and oxygenation will be developed into a predictive *in silico* model aimed at forecasting morphological changes. Physiological equations and previous *in vivo* experiments will be integrated into the model. The model will calculate probable progression of angiogenic and arteriogenic processes in a mouse model. Images will be taken and quantified on a day 0 time-point. Vascular data will be used in the model to predict growth of vessels and compared to future measurements. Vascular modulating therapy will be tested as well in the model.

Microvascular quantification has implications in preclinical research of many diseases, including solid tumors, retinopathy, peripheral arterial disease, and ischemic stroke. Optical techniques allow for longitudinal monitoring of dynamic vasculature. Contrasting predictive model endpoints with measured endpoints can help describe physiological changes induced by vascular therapies. This research will have broad application in preclinical vascular models, and will have a strong focus on relating physiological modeling to vascular disease state and therapy.

REFERENCES

[1] M. E. Swift, H. K. Kleinman, and L. A. DiPietro, “Impaired wound repair and delayed angiogenesis in aged mice.,” *Lab. Invest.*, vol. 79, no. 12, pp. 1479–87, Dec. 1999.

[2] M. Potente, H. Gerhardt, and P. Carmeliet, “Basic and therapeutic aspects of angiogenesis.,” *Cell*, vol. 146, no. 6, pp. 873–87, Sep. 2011.

[3] J. Llevadot and T. Asahara, “Effects of statins on angiogenesis and vasculogenesis.,” *Rev. española Cardiol.*, vol. 55, no. 8, pp. 838–44, Aug. 2002.

[4] P. Carmeliet, “Angiogenesis in life, disease and medicine,” *Nature*, 2005.

[5] J. Folkman, “Role of angiogenesis in tumor growth and metastasis,” *Semin. Oncol.*, vol. 29, no. 6, pp. 15–18, Dec. 2002.

[6] R. K. Jain, “Normalizing tumor vasculature with anti-angiogenic therapy: a new paradigm for combination therapy.,” *Nat. Med.*, vol. 7, no. 9, pp. 987–9, Sep. 2001.

[7] R. K. Jain, “Normalizing tumor microenvironment to treat cancer: bench to bedside to biomarkers.,” *J. Clin. Oncol.*, vol. 31, no. 17, pp. 2205–18, Jun. 2013.

[8] M. E. Hardee, R. J. Eapen, Z. N. Rabbani, M. R. Dreher, J. Marks, K. L. Blackwell, and M. W. Dewhirst, “Her2/neu signaling blockade improves tumor oxygenation in a multifactorial fashion in Her2/neu+ tumors.,” *Cancer Chemother. Pharmacol.*, vol. 63, no. 2, pp. 219–28, Jan. 2009.

[9] G. Shen, H. Huang, A. Zhang, T. Zhao, S. Hu, L. Cheng, J. Liu, W. Xiao, B. Ling, Q. Wu, L. Song, and W. Wei, “In vivo activity of novel anti-ErbB2 antibody chA21 alone and with Paclitaxel or Trastuzumab in breast and ovarian cancer xenograft models.,” *Cancer Immunol. Immunother.*, vol. 60, no. 3, pp. 339–48, Mar. 2011.

[10] C. Shah, T. W. Miller, S. K. Wyatt, E. T. McKinley, M. G. Olivares, V. Sanchez, D. D. Nolting, J. R. Buck, P. Zhao, M. S. Ansari, R. M. Baldwin, J. C. Gore, R. Schiff, C. L. Arteaga, and H. C. Manning, “Imaging biomarkers predict response to anti-HER2 (ErbB2) therapy in preclinical models of breast cancer.,” *Clin. Cancer Res.*, vol. 15, no. 14, pp. 4712–21, Jul. 2009.

[11] C. V Pastuskovas, E. E. Mundo, S. P. Williams, T. K. Nayak, J. Ho, S. Ulufatu, S. Clark, S. Ross, E. Cheng, K. Parsons-Reponte, G. Cain, M. Van Hoy, N. Majidy, S. Bheddah, J. dela Cruz Chuh, K. R. Kozak, N. Lewin-Koh, P. Nauka, D. Bumbaca, M. Sliwkowski, J. Tibbitts, F.-P. Theil, P. J. Fielder, L. a Khawli, and C. A. Boswell, “Effects of anti-VEGF on pharmacokinetics, biodistribution, and tumor penetration of trastuzumab in a

preclinical breast cancer model.," *Mol. Cancer Ther.*, vol. 11, no. 3, pp. 752–62, Mar. 2012.

[12] J. F. De Los Santos, A. Cantor, K. D. Amos, A. Forero, M. Golshan, J. K. Horton, C. A. Hudis, N. M. Hylton, K. McGuire, F. Meric-Bernstam, I. M. Meszoely, R. Nanda, and E. S. Hwang, "Magnetic resonance imaging as a predictor of pathologic response in patients treated with neoadjuvant systemic treatment for operable breast cancer. Translational Breast Cancer Research Consortium trial 017.," *Cancer*, vol. 119, no. 10, pp. 1776–83, May 2013.

[13] H. Degani, M. Chetrit-Dadiani, L. Bogin, and E. Furman-Haran, "Magnetic resonance imaging of tumor vasculature.," *Thromb. Haemost.*, vol. 89, no. 1, pp. 25–33, Jan. 2003.

[14] R. K. Jain, "Normalization of tumor vasculature: an emerging concept in antiangiogenic therapy.," *Science*, vol. 307, no. 5706, pp. 58–62, Jan. 2005.

[15] J. S. Ross and J. A. Fletcher, "The HER-2/neu oncogene in breast cancer: prognostic factor, predictive factor, and target for therapy.," *Stem Cells*, vol. 16, no. 6, pp. 413–28, Jan. 1998.

[16] W. Liu, J. Li, and R. a Roth, "Heregulin regulation of Akt/protein kinase B in breast cancer cells.," *Biochem. Biophys. Res. Commun.*, vol. 261, no. 3, pp. 897–903, Aug. 1999.

[17] E. Laughner, P. Taghavi, K. Chiles, P. C. Mahon, and G. L. Semenza, "HER2 (neu) signaling increases the rate of hypoxia-inducible factor 1α (HIF-1α) synthesis: novel mechanism for HIF-1-mediated vascular endothelial growth factor expression," *Mol. Cell. Biol.*, vol. 21, no. 12, pp. 3995–4004, 2001.

[18] D. Slamon, W. Godolphin, L. Jones, J. Holt, S. Wong, D. Keith, W. Levin, S. Stuart, J. Udove, A. Ullrich, and al. et, "Studies of the HER-2/neu proto-oncogene in human breast and ovarian cancer," *Science (80-.).*, vol. 244, no. 4905, pp. 707–712, May 1989.

[19] R. K. Tiwari, P. I. Borgen, G. Y. Wong, C. Cordon-Cardo, and M. P. Osborne, "HER-2/neu amplification and overexpression in primary human breast cancer is associated with early metastasis.," *Anticancer Res.*, vol. 12, no. 2, pp. 419–25, Jan. 1992.

[20] B. R. Seshadri, F. A. Firgaira, D. J. Horsfall, K. Mccaul, V. Setlur, and P. Kitchen, "Clinical Significance of HER-2 / neu Oncogene Amplification in Primary Breast Cancer," vol. 11, no. 10, pp. 1936–1942, 2014.

[21] D. Slamon, B. Leyland-Jones, S. Shak, H. Fuchs, V. Paton, A. Bajamonde, T. Fleming, W. Eiermann, J. Wolter, M. Pegram, J. Baselga, and L. Norton, "Use of chemotherapy plus a monoclonal antibody against HER2 for metastatic breast cancer that overexpresses HER2," *N. Engl. J. Med.*, vol. 344, no. 11, pp. 783–792, 2001.

[22] C. L. Vogel, M. A. Cobleigh, D. Tripathy, J. C. Gutheil, L. N. Harris, L. Fehrenbacher, D. J. Slamon, M. Murphy, W. F. Novotny, M. Burchmore, S. Shak, S. J. Stewart, and M. Press, "Efficacy and Safety of Trastuzumab as a Single Agent in First-Line Treatment of HER2-Overexpressing Metastatic Breast Cancer," *J. Clin. Oncol.*, vol. 20, no. 3, pp. 719–726, Feb. 2002.

[23] G. Valabrega, F. Montemurro, and M. Aglietta, "Trastuzumab: mechanism of action, resistance and future perspectives in HER2-overexpressing breast cancer.," *Ann. Oncol.*, vol. 18, no. 6, pp. 977–84, Jun. 2007.

[24] Y. Izumi, L. Xu, E. di Tomaso, D. Fukumura, and R. K. Jain, "Tumour biology: herceptin acts as an anti-angiogenic cocktail.," *Nature*, vol. 416, no. 6878, pp. 279–80, Mar. 2002.

[25] A. Mariampillai and B. Standish, "Speckle variance detection of microvasculature using swept-source optical coherence tomography," *Opt. …*, 2008.

[26] S. Yazdanfar, M. Kulkarni, and J. Izatt, "High resolution imaging of in vivo cardiac dynamics using color Doppler optical coherence tomography," *Opt. Express*, 1997.

[27] J. Izatt, M. Kulkarni, and S. Yazdanfar, "< i> In vivo</i> bidirectional color Doppler flow imaging of picoliter blood volumes using optical coherence tomography," *Opt. …*, 1997.

[28] D. B. Jakubowski, A. E. Cerussi, F. Bevilacqua, N. Shah, D. Hsiang, J. Butler, and B. J. Tromberg, "Monitoring neoadjuvant chemotherapy in breast cancer using quantitative diffuse optical spectroscopy: a case study.," *J. Biomed. Opt.*, vol. 9, no. 1, pp. 230–8, 2004.

[29] A. Cerussi, D. Hsiang, N. Shah, R. Mehta, A. Durkin, J. Butler, and B. J. Tromberg, "Predicting response to breast cancer neoadjuvant chemotherapy using diffuse optical spectroscopy.," *Proc. Natl. Acad. Sci. U. S. A.*, vol. 104, no. 10, pp. 4014–9, Mar. 2007.

[30] F. Bevilacqua, a J. Berger, a E. Cerussi, D. Jakubowski, and B. J. Tromberg, "Broadband absorption spectroscopy in turbid media by combined frequency-domain and steady-state methods.," *Appl. Opt.*, vol. 39, no. 34, pp. 6498–507, Dec. 2000.

[31] X. Wang, X. Xie, G. Ku, L. V Wang, and G. Stoica, "Noninvasive imaging of hemoglobin concentration and oxygenation in the rat brain using high-resolution photoacoustic tomography.," *J. Biomed. Opt.*, vol. 11, no. 2, p. 024015, 2006.

[32] J. Laufer, P. Johnson, E. Zhang, B. Treeby, B. Cox, B. Pedley, and P. Beard, "In vivo preclinical photoacoustic imaging of tumor vasculature development and therapy.," *J. Biomed. Opt.*, vol. 17, no. 5, p. 056016, May 2012.

[33] B. S. Sorg, B. J. Moeller, O. Donovan, Y. Cao, and M. W. Dewhirst, "Hyperspectral imaging of hemoglobin saturation in tumor microvasculature and tumor hypoxia development.," *J. Biomed. Opt.*, vol. 10, no. 4, p. 44004, 2005.

[34] G. M. Palmer, A. N. Fontanella, G. Zhang, G. Hanna, C. L. Fraser, and M. W. Dewhirst, "Optical imaging of tumor hypoxia dynamics.," *J. Biomed. Opt.*, vol. 15, no. 6, p. 066021, 2010.

[35] G. M. Palmer, A. N. Fontanella, S. Shan, G. Hanna, G. Zhang, C. L. Fraser, and M. W. Dewhirst, "In vivo optical molecular imaging and analysis in mice using dorsal window chamber models applied to hypoxia, vasculature and fluorescent reporters.," *Nat. Protoc.*, vol. 6, no. 9, pp. 1355–66, Sep. 2011.

[36] G. M. Palmer, R. J. Viola, T. Schroeder, P. S. Yarmolenko, M. W. Dewhirst, and N. Ramanujam, "Quantitative diffuse reflectance and fluorescence spectroscopy: tool to monitor tumor physiology in vivo.," *J. Biomed. Opt.*, vol. 14, no. 2, p. 024010, Jan. 2009.

[37] A. Helisch, S. Wagner, N. Khan, M. Drinane, S. Wolfram, M. Heil, T. Ziegelhoeffer, U. Brandt, J. D. Pearlman, H. M. Swartz, and W. Schaper, "Impact of mouse strain differences in innate hindlimb collateral vasculature.," *Arterioscler. Thromb. Vasc. Biol.*, vol. 26, no. 3, pp. 520–6, Mar. 2006.

[38] R. D. Shonat, E. S. Wachman, W. Niu, A. P. Koretsky, and D. L. Farkas, "Near-simultaneous hemoglobin saturation and oxygen tension maps in mouse brain using an AOTF microscope," 1997.

[39] R. L. Greenman, S. Panasyuk, X. Wang, T. E. Lyons, T. Dinh, L. Longoria, J. M. Giurini, J. Freeman, L. Khaodhiar, and A. Veves, "Early changes in the skin microcirculation and muscle metabolism of the diabetic foot.," *Lancet*, vol. 366, no. 9498, pp. 1711–7, Nov. 2005.

[40] M. a Afromowitz, J. B. Callis, D. M. Heimbach, L. a DeSoto, and M. K. Norton, "Multispectral imaging of burn wounds: a new clinical instrument for evaluating burn depth.," *IEEE Trans. Biomed. Eng.*, vol. 35, no. 10, pp. 842–50, Oct. 1988.

[41] L. C. Cancio, A. I. Batchinsky, J. R. Mansfield, S. Panasyuk, K. Hetz, D. Martini, B. S. Jordan, B. Tracey, and J. E. Freeman, "Hyperspectral imaging: a new approach to the diagnosis of hemorrhagic shock.," *J. Trauma*, vol. 60, no. 5, pp. 1087–95, May 2006.

[42] R. Siegel, D. Naishadham, and A. Jemal, "Cancer Statistics , 2013," vol. 63, no. 1, pp. 11–30, 2013.

[43] M. J. Piccart-Gebhart, M. Procter, B. Leyland-Jones, A. Goldhirsch, M. Untch, I. Smith, L. Gianni, J. Baselga, R. Bell, C. Jackisch, D. Cameron, M. Dowsett, C. H. Barrios, G. Steger, C.-S. Huang, M. Andersson, M. Inbar, M. Lichinitser, I. Láng, U. Nitz, H. Iwata, C. Thomssen, C. Lohrisch, T. M. Suter, J. Rüschoff, T. Sütő, V. Greatorex, C. Ward, C. Straehle, E. McFadden, M. S. Dolci, and R. D. Gelber, "Trastuzumab after Adjuvant Chemotherapy in HER2-Positive Breast Cancer," *N. Engl. J. Med.*, vol. 353, no. 16, pp. 1659–1672, 2005.

[44] M. W. Dewhirst, “Relationships between cycling hypoxia, HIF-1, angiogenesis and oxidative stress.,” *Radiat. Res.*, vol. 172, no. 6, pp. 653–65, Dec. 2009.

[45] “Efficacy and Safety of Trastuzumab as a Single Agent in Metastatic First-line Treatment Her-overexpressing,” vol. 20, no. 3, pp. 719–726, 2003.

[46] S. H. Park, W. K. Moon, N. Cho, J. M. Chang, S.-A. Im, I. A. Park, K. W. Kang, W. Han, and D.-Y. Noh, “Comparison of diffusion-weighted MR imaging and FDG PET/CT to predict pathological complete response to neoadjuvant chemotherapy in patients with breast cancer.,” *Eur. Radiol.*, vol. 22, no. 1, pp. 18–25, Jan. 2012.

[47] K. J. Zuzak, M. D. Schaeberle, E. N. Lewis, and I. W. Levin, “Visible Reflectance Hyperspectral Imaging: Characterization of a Noninvasive, in Vivo System for Determining Tissue Perfusion,” *Anal. Chem.*, vol. 74, no. 9, pp. 2021–2028, May 2002.

[48] A. N. Fontanella, “Novel Methods of Optical Data Analysis to Assess Radiation Responses in the Tumor Microenvironment,” Duke University, 2013.

[49] B. J. Vakoc, R. M. Lanning, J. a Tyrrell, T. P. Padera, L. a Bartlett, T. Stylianopoulos, L. L. Munn, G. J. Tearney, D. Fukumura, R. K. Jain, and B. E. Bouma, “Three-dimensional microscopy of the tumor microenvironment in vivo using optical frequency domain imaging.,” *Nat. Med.*, vol. 15, no. 10, pp. 1219–23, Oct. 2009.

[50] C. A. Ritter, M. Perez-Torres, C. Rinehart, M. Guix, T. Dugger, J. a Engelman, and C. L. Arteaga, “Human breast cancer cells selected for resistance to trastuzumab in vivo overexpress epidermal growth factor receptor and ErbB ligands and remain dependent on the ErbB receptor network.,” *Clin. Cancer Res.*, vol. 13, no. 16, pp. 4909–19, Aug. 2007.

[51] H. C. Hendargo, R. Estrada, S. J. Chiu, C. Tomasi, S. Farsiu, and J. a. Izatt, “Automated non-rigid registration and mosaicing for robust imaging of distinct retinal capillary beds using speckle variance optical coherence tomography,” *Biomed. Opt. Express*, vol. 4, no. 6, p. 803, May 2013.

[52] P. Santago and H. D. Gage, “Quantification of MR brain images by mixture density and partial volume modeling.,” *IEEE Trans. Med. Imaging*, vol. 12, no. 3, pp. 566–74, Jan. 1993.

[53] H. Akaike, “A new look at the statistical model identification,” *IEEE Trans. Automat. Contr.*, vol. 19, no. 6, pp. 716–723, Dec. 1974.

[54] G. Brockhoff, B. Heckel, E. Schmidt-Bruecken, M. Plander, F. Hofstaedter, a Vollmann, and S. Diermeier, “Differential impact of Cetuximab, Pertuzumab and Trastuzumab on BT474 and SK-BR-3 breast cancer cell proliferation.,” *Cell Prolif.*, vol. 40, no. 4, pp. 488–507, Aug. 2007.

[55] G. D. Yancopoulos, S. Davis, N. W. Gale, J. S. Rudge, S. J. Wiegand, and J. Holash, "Vascular-specific growth factors and blood vessel formation.," *Nature*, vol. 407, no. 6801, pp. 242–8, Sep. 2000.

[56] J. O. A. Forsythe, B. Jiang, N. V Iyer, F. Agani, and S. W. Leung, "Activation of vascular endothelial growth factor gene transcription by hypoxia-inducible factor Activation of Vascular Endothelial Growth Factor Gene Transcription by Hypoxia-Inducible Factor 1," 1996.

[57] A. J. Walsh, R. S. Cook, H. C. Manning, D. J. Hicks, A. Lafontant, C. L. Arteaga, and M. C. Skala, "Optical metabolic imaging identifies glycolytic levels, subtypes, and early-treatment response in breast cancer.," *Cancer Res.*, vol. 73, no. 20, pp. 6164–74, Oct. 2013.